

## ARTICLE OPEN

## Structure of International Simple Glass and properties of passivating layer formed in circumneutral pH conditions

Marie Collin<sup>1</sup>, Maxime Fournier<sup>1</sup>, Pierre Frugier<sup>1</sup>, Thibault Charpentier<sup>2</sup>, Mélanie Moskura<sup>2</sup>, Lu Deng<sup>3</sup>, Mengguo Ren<sup>3</sup>, Jincheng Du<sup>3</sup> and Stéphane Gin<sup>1</sup>

Knowing the structure of a material is necessary to understand its evolution under various influences; here, the alteration by water of a reference glass of nuclear interest, called International Simple Glass (ISG), is studied. The ISG atomic structure has not yet been thoroughly characterized. Short- and medium-range order in this six-oxide glass was investigated by molecular dynamics (MD) methods. Combining the simulated data with experimental observations acquired from both pristine and altered ISG provided new insight into the formation of surface layers and passivation of the underlying glass. In the tested conditions of 90 °C, silica-saturated solution, and pH<sub>90°C</sub> 7, the passivating layer partly inherits the structure of the pristine glass network despite the release of mobile elements (Na, B, and some Ca), with a reorganization of the silicate network following B release. The layer appears to minimize its internal energy by relaxing strain accumulated during glass quenching. The resulting passivated glass shows a strong resistance to hydrolysis. The nanopores of this hydrated material, displaying a mean pore size of ~1 nm, are filled with various water species. Water speciation determination inside the nanopores is therefore an achievement for future water dynamic study in the passivated glass.

*npj Materials Degradation* (2018)2:4; doi:10.1038/s41529-017-0025-y

## INTRODUCTION

At a time when climate change causes many societal issues, the nuclear industry is a controversial topic, as many advocate for a transition to renewable energy. Nuclear power is carbon-neutral, but accidents such as Chernobyl and Fukushima Daiichi have contributed significantly to public concern. Regardless of public opinion, nuclear energy use in the last 60 years has already produced toxic nuclear wastes. Most require conditioning and safe management. Currently, high-level radioactive waste arising from reprocessing is vitrified. Countries producing such borosilicate glass waste form have selected deep geological repositories as long-term solutions to dispose of these materials.<sup>1</sup> Thus, many studies are conducted on the long-term behavior of the glass obtained by vitrification of radioactive waste, intended to develop reliable predictive glass corrosion models.<sup>1–4</sup>

International Simple Glass (ISG) has become a reference borosilicate glass in the past few years for such studies.<sup>1</sup> Its simplified six-oxide composition is a good analog of R7T7 glass, the multiple-oxide glass produced from the reprocessing of French spent fuels. The atomic structure of pristine ISG glass remains partly unknown, although many alteration and irradiation studies have been conducted on it in recent years.<sup>5–10</sup> The structure of a glass is related to the internal energy of glass formation. Recently, the entropy relating to the degree of disorder within the glassy structure was demonstrated to affect the glass dissolution kinetics at low reaction progress.<sup>11</sup> This indicates the necessity of a better understanding of the glass structure. Some structural information, such as boron speciation, is already known.<sup>7</sup>  $Q^n$  distribution ( $n$  refers to the number of bridging O

around a network former cation), on the contrary, has never been determined because of the highly complex signals obtained with nuclear magnetic resonance (NMR) spectroscopy.<sup>7,8</sup> Classical molecular dynamics (MD) simulations can provide detailed information on the short- and medium-range structural order in multi-oxide glasses.<sup>12,13</sup> In the past, binary<sup>14</sup> and ternary glasses have been successfully simulated using MD.<sup>15,16</sup> Multicomponent glasses require the use of composition-dependent parameters that necessitate experimental validation.<sup>17,18</sup> In this study, the pristine ISG structure was successfully simulated using new partial-charge pairwise potentials, providing previously unknown structural information.

Understanding the pristine glass structure is the first step to better understand glass alteration. However, despite studies of glass alteration in recent decades, the coupling of the basic mechanisms, including ion exchange, hydrolysis of covalent bonds, condensation of partly hydrolyzed species, structural relaxation, transport of hydrogenated species through forming layer, and precipitation of secondary minerals, remains unclear. It is therefore necessary to study layers formed at low and high reaction progresses separately to better understand the rate-controlling mechanisms acting in each case.<sup>19</sup> Previous experiments performed in <sup>29</sup>Si saturated solution at pH<sub>90°C</sub> 7 and 9<sup>5,8</sup> demonstrated that the passivation layers formed in these conditions partly inherited the structure of the pristine glass skeleton. The alteration rate appeared to be limited by the accessibility of water molecules to the reactive interface. Because water exists as various species within the altered glass layer, mainly as water molecules and hydroxyl groups,<sup>20</sup> this raises questions regarding the repartition and mobility of these species.

<sup>1</sup>CEA, DEN, DE2D, SEVT, Bagnols-sur-Ceze F-30207, France; <sup>2</sup>NIMBE, CEA, CNRS, Université Paris-Saclay, CEA Saclay, Gif-sur-Yvette Cedex, Paris 91191, France and <sup>3</sup>Department of Materials Science and Engineering, University of North Texas, Denton, TX, USA  
Correspondence: Stéphane Gin (stephane.gin@cea.fr)

Received: 12 July 2017 Revised: 21 November 2017 Accepted: 12 December 2017

Published online: 05 February 2018

**Table 1.** MD simulations data

Q <sup>n</sup> distribution											
X	n=	2	3	4	5	6	7				
Si		0.5 ± 0.1	13.8 ± 0.3	85.7 ± 0.1	–	–	–				
B		3.7 ± 0.4	39.4 ± 0.5	56.8 ± 0.5	–	–	–				
Al		–	2.5 ± 0.2	96.7 ± 0.1	0.9 ± 0.2	–	–				
Zr		–	–	–	13.0 ± 0.8	83.4 ± 0.3	3.6 ± 0.7				
X	<i>r</i> <sub>x–o</sub> (Å)	<i>r</i> <sub>cut</sub> (Å)	CN <sub>avg</sub>	Coordination Number (CN) distribution (%)							
				3	4	5	6	7	8	9	≥ 10
Si	1.61	2.25	4.00	–	100 ± 0.0	–	–	–	–	–	–
B	1.45 (B <sup>[3]</sup> ) 1.55 (B <sup>[4]</sup> )	2.00	3.59	41.3 ± 0.5	58.7 ± 0.5	–	–	–	–	–	–
Al	1.77	2.25	4.00	0.5 ± 0.2	98.6 ± 0.2	0.9 ± 0.2	–	–	–	–	–
Zr	2.10	2.85	5.68	–	–	10.7 ± 1.2	85.7 ± 0.6	3.6 ± 0.7	–	–	–
Na	2.47	3.30	7.42	0.1 ± 0.1	0.6 ± 0.1	5.9 ± 0.5	17.6 ± 0.9	28.1 ± 0.6	27.5 ± 0.6	15.4 ± 1.4	3.5 ± 1.9
Ca	2.42	3.10	6.62	–	1.8 ± 0.8	11.2 ± 1.7	32.9 ± 3.3	34.3 ± 2.3	16.1 ± 0.4	3.5 ± 0.6	–
O	2.59	2.925	–	–	–	–	–	–	–	–	–

Q<sup>n</sup> distribution for network former. Bond length *r*<sub>x–o</sub>, cutoff used for CN calculation (*r*<sub>cut</sub>), cation-averaged coordination number (CN<sub>avg</sub>) and corresponding CN distributions in ISG. X are elements in the ISG composition

For this study, the conditions of pH<sub>90°C</sub> 7 in a solution saturated with amorphous silica were set. These starting conditions circumvent the silicate network dissolution that typically occurs early in glass corrosion. Glass alteration was therefore driven only by the transport of water through the growing alteration layer and the reaction of water with mobile cations within the glass (mainly B, Na, and Ca). The glass alteration kinetics was measured and the pristine and altered glass compositions were determined by both chemical analysis and time-of-flight secondary-ion mass spectroscopy (ToF-SIMS) profiling. NMR spectroscopy was performed to compare the pristine and altered glasses and to validate the MD simulation. The resulting data demonstrated the inheritance of the pristine glass network by the passivation layers in the specified conditions as well as repolymerization of this boron-free network after mobile species release. Water speciation in the hydrated ISG was studied quantitatively by combining thermogravimetric analysis (TGA) and NMR methods, which may facilitate water dynamic studies in the nanochannels formed by glass alteration.

## RESULTS

### MD simulations

The ISG structure was simulated to obtain an internal view of its atomic-scale structure. All the glass-forming cations and O atoms are well mixed without obvious phase separation (see Supplementary Material Fig. S1a and b). Structure-related properties, such as the total correlation function (TCF, *T(r)*), pair distribution function (PDF, *g(r)*), coordination number (CN), and bond-angle distribution (BAD) were calculated. The Q<sup>n</sup> distribution was determined for each network former of Si, B, Al, and Zr (Table 1). The number of non-bridging O (NBO) atoms around each Si atom was also calculated, and the concentration of NBO bound to Si was estimated at ~3.7%. The TCF and CN are presented in the Supplementary Material (Fig. S1c and d). The bond length of each pair was determined from the first peak position in the corresponding TCF. The average CNs, the cutoff values used for CN calculation, and the corresponding cation–oxygen bond lengths are summarized in Table 1. The

TCF and BAD of O–B–O, displayed in Fig. 1a and b, highlight the presence of two boron coordination species of B<sup>[3]</sup> and B<sup>[4]</sup>. Based on the MD simulation results, the ratio of B<sup>[4]</sup>/(B<sup>[3]</sup> + B<sup>[4]</sup>) is 0.59.

ISG contains several glass formers, namely Zr, Al, and B, that form negatively charged units of [ZrO<sub>6</sub>]<sup>2–</sup>, [AlO<sub>4</sub>]<sup>–</sup>, and [BO<sub>4</sub>]<sup>–</sup>, respectively. Ca<sup>2+</sup> and Na<sup>+</sup> compensate for these negative charges, but the cation species for preferential charge compensation remains unclear; however, it can be determined by comparing the PDFs shown in Fig. 1c–e, as higher peak intensities indicate higher probabilities of presence. For the B–Ca, Al–Ca, and Zr–Ca PDFs, the Zr–Ca pair clearly possesses the highest first-peak intensity, indicating that Ca is more often associated with Zr than with B or Al. Moreover, the first PDF peak intensity of Zr–Na is lower than that of Zr–Ca in Fig. 1e, further illustrating that Zr is preferentially compensated by Ca rather than Na. This disagrees with experimental data, as discussed later.

Three distinct peaks occur in the distance range of 3.0 to 4.5 Å in the Zr–Ca PDF. By decomposing the Zr–Ca contributions to 5-, 6-, and 7-coordinated Zr (see Supplementary Material Fig. S1f), the majority of the contribution can be assigned to Zr<sup>[6]</sup>–Ca, while Zr<sup>[5]</sup>–Ca contributes only to the formation of the second peak and the contribution of Zr<sup>[7]</sup>–Ca is negligible because of the low concentration of Zr<sup>[7]</sup>.

It is less clear whether Ca or Na is favored for Al charge compensation, as the Al–Na and Al–Ca PDF peaks displayed in Fig. 1d are similar in intensity. Similarly, when comparing Si/B/Al/Zr–Na PDF peak intensities, no signal is clearly distinguished from the others (see Supplementary Material Fig. S1e). Na does not seem to show preferential association with any of these elements.

To complete this study of simulated pristine ISG, the ring size distribution is calculated for medium-range structural analysis. In ISG, Si, B, Al, and Zr can be considered glass-former cations. When all four species are considered, the ring size distribution shows a symmetric Gaussian-type distribution with a peak centered at seven-membered rings, suggesting that when all network formers are considered, the structure resembles a three-dimensional random network. Leaving Zr out of the calculation, the ring size distribution does not change, possibly because of the low ZrO<sub>2</sub>

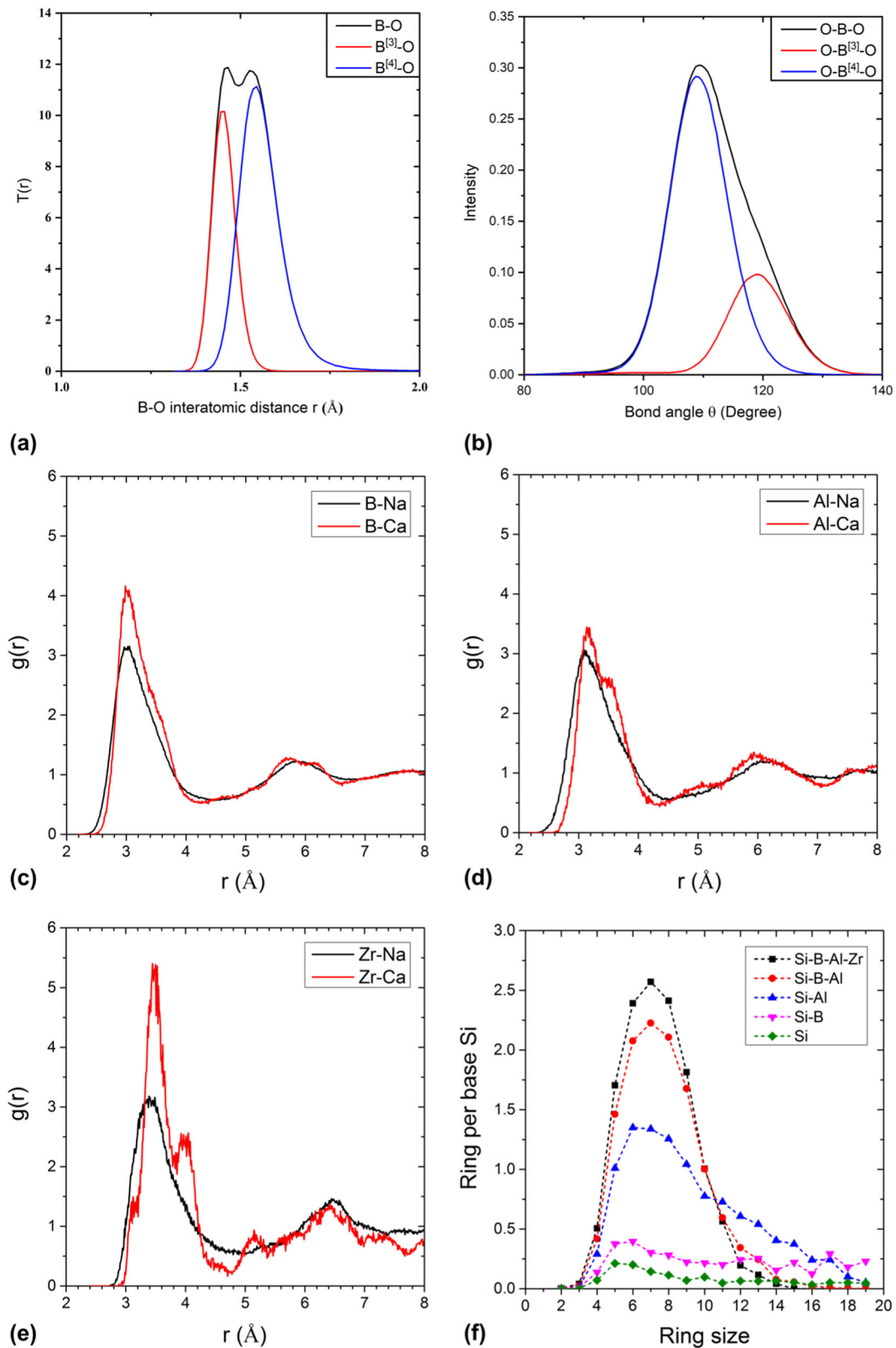


**Fig. 1** MD simulations of ISG structure. Deconvolution of **a** TCF of B-O and **b** BAD of O-B-O in the simulated ISG structure. **c** B-Ca/Na PDF. **d** Al-Ca/Na PDF. **e** Zr-Ca/Na PDF. **f** Ring size distribution calculated for different ISG glass formers

molar content in ISG. Omitting both Zr and B decreases the ring size distribution peak intensity and produces a tail for larger rings. Finally, when considering Si and B, or only Si, the network is much more fragmented with a wide distribution of rings. All these

results are depicted in Fig. 1f. This suggests that B connects the Si and Al networks in the glass. This has important implications for chemical durability, as B is a highly hydrolyzable species. This therefore suggests that the network remaining after B release

could be fragmented and prone to recondensation. This is coherent with the NBO percentage (43.8% of O) calculated from ISG composition after B release (Table 2).

#### Alteration kinetics

ISG glass powder of 20–40 μm in particle size was altered at neutral pH in silica-saturated conditions. As shown in Fig. 2, the glass is altered despite the high concentration of Si in the solution. The Si concentration in solution remains constant over time ( $C(\text{Si}) = 142 \pm 6 \text{ mg L}^{-1}$ ), whereas the Al and Zr concentrations remain below the detection limit (<0.10 ppm), suggesting that the Al–Zr–silicate network is potentially reorganized but not dissolved. In such conditions, only mobile cations such as B, Na, and Ca are leached from ISG.

The 20–40-μm-sized glass powder reached near total alteration (~90–95% of B leached from ISG) after 250 days, corresponding to an equivalent thickness  $ET(\text{B}) \approx 7.3 \mu\text{m}$  calculated from the B concentration. The shape of the curve indicates a significant decrease in the alteration rate over time, with a drop from ~340 nm day<sup>-1</sup> on the first day to ~10 nm day<sup>-1</sup> after 250 days

(see Supplementary Material Fig. S2b).  $ET(\text{B})$  is well correlated with  $t^{1/2}$  (see Fig. 2b), indicating that the release of mobile species (B and Na, which are congruently released from the glass as shown in Fig. 2a) is diffusion-limited through the growing alteration layer. Although the rate-limiting process controlling diffusion must not be inferred from this approach, an apparent diffusion coefficient  $D_{\text{B}}^{\text{Fick}}$  of  $2 \times 10^{-18} \text{ m}^2 \cdot \text{s}^{-1}$  can nonetheless be derived from the solution to Fick's second law (refer to Supplementary Material part 3 for the resolution of this solution):

$$ET(\text{B}) = \frac{2}{\sqrt{\pi}} \sqrt{D_{\text{B}}^{\text{Fick}} t} \quad (1)$$

#### Solid analysis

**Chemical analysis.** A comparison of 3.5–5.5 μm pristine and altered glass powder compositions is shown in Table 2. As expected from the solution analysis, B and Na are removed, while significant Ca (71%) remains in the altered material. Small amounts of K appear, attributed to the use of the pH electrode; a K concentration reaching  $19 \text{ mg L}^{-1}$  is detected in solution at

**Table 2.** Experimental data obtained on pristine and altered glass

Composition (At%)		Pristine Glass											Altered glass										
		Si	B	Na	K	Al	Ca	Zr	O	Si/Zr	Al/Zr	Charge	Si	B	Na	K	Al	Ca	Zr	O	Si/Zr	Al/Zr	Charge
		18.0	9.6	7.5	-	2.3	1.7	0.5	60.3	36	5	+3	28.9	0.4	0.4	0.7	3.6	1.9	0.7	63.3	40	5	0
Error ±		-	-	-	-	-	-	-	-	-	-	-	5.4	0.1	0.1	0.1	0.6	0.4	0.0	11.4	-	-	-
Density (g·cm <sup>-3</sup> )	Model 1	2.5 ± 0.5											2.3 ± 0.4										
	Model 2	-											2.1 ± 0.4										
Initial dissolution rate (g·m <sup>-2</sup> ·d <sup>-1</sup> )	Replicate 1	0.90 ± 0.18											0.08 ± 0.02										
	Replicate 2	1.01 ± 0.20											0.09 ± 0.02										
	Mean value	0.96 ± 0.19											0.09 ± 0.02										
	σ	0.08											0.01										
Total water content (Wt%)		1.2 ± 0.01											16.5 ± 0.2										
<b>Altered glass water loss</b>																							
														Temperature (°C)		Water loss Total water content (%)							
														25 to 90		34							
														90 to 150		24							
														150 to 300		24							
														300 to 450		11							
														450 to 1200		7							
<b>Altered glass water speciation</b>																							
Proton repartition (% of H)																							
H of -X-OH <sub>HB</sub>														H of H <sub>2</sub> O <sub>mol</sub>		H of "free" -X-OH							
29 ± 3														68 ± 7		3 ± 0.3							
O <sub>BO</sub>														O of H <sub>2</sub> O <sub>mol</sub>		O <sub>NBO</sub>							
63 ± 11														19 ± 3		18 ± 3							
Oxygen repartition in the skeleton (% of O)																							
Pristine glass														95.5		4.5							
Pristine glass - after boron release														56.2		43.8							
Altered glass														78		22							
<b>Altered glass porosity parameters</b>																							
Mobile elements departure														Specific surface area (m <sup>2</sup> ·g <sup>-1</sup> )		"Free" volume (%)		Mean pore diameter (nm)					
TGA and NMR														-		33.5 ± 6.0		-					
Effective (H <sub>2</sub> O)														716 ± 129		27.9 ± 5.0		0.9 ± 0.2					
Total (H <sub>2</sub> O + "free" -X-OH + -X-OH <sub>HB</sub> )														-		54.6 ± 9.8		1.8 ± 0.3					

Glass composition: Si, B, Na, K, Al, Ca, and Zr concentrations were obtained by inductively Coupled Plasma Atomic Emission Spectroscopy (ICP-AES) analysis with uncertainties of 10%, and O was calculated using Eq. 9. The charge balance was obtained as described by Angeli et al.<sup>22</sup>. Density: densities are calculated from the pristine and altered glass compositions. Two models were used. Model 1 was developed by Fluegel<sup>29</sup> for pristine glasses and does not consider water. Model 2, developed by Iacovino<sup>30</sup>, was designed for hydrated melts and does not consider B, and therefore cannot be applied to the pristine glass. Initial dissolution rate:  $r_0$  were determined at pH<sub>90 °C</sub> 7, according to Si release in extremely diluted conditions. Total water content/Altered glass water loss: water quantification in pristine and altered glass is extracted from TGA analysis. Altered glass water speciation: proton repartition in the altered glass was obtained from 1H NMR spectrum deconvolution. Using this proton repartition, the oxygen repartitions were determined in the altered glass structure (refer to Supplementary Material part 7–8 for more information). Altered glass porosity parameters: the specific surface area and volume of the porosity are calculated from TGA and NMR data. The mean pore diameter is calculated assuming perfectly spherical nanopores (refer to Supplementary Material part 7 for more information)

Bold values are the mean values for initial dissolution rate is the mean value between replicate 1 and 2, while  $\sigma$  is the standard deviation between the replicate

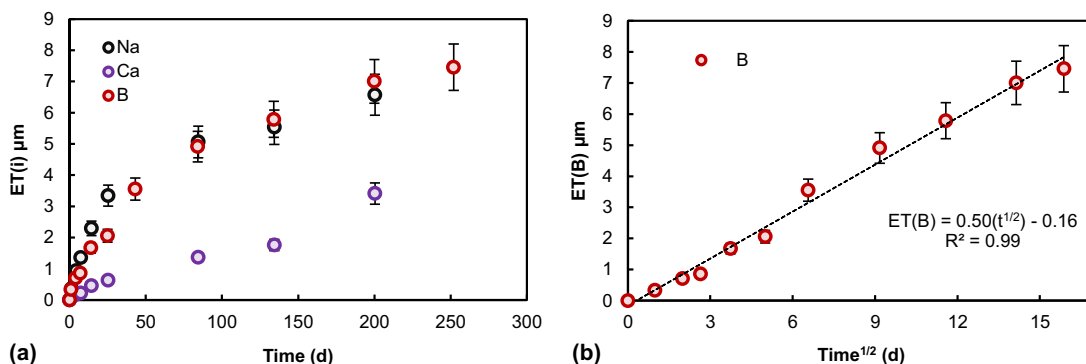


**Fig. 2** Data from solution analysis. **a** Equivalent thickness  $ET(i)$  (where  $i = B, Na,$  and  $Ca$ ) calculated from Eq. 6. Outliers such as  $Na$  and  $Ca$  last points were removed. The equivalent thicknesses calculated at 25 and 134 days are consistent with SEM imaging and ToF-SIMS depth profiling (see Supplementary Material Fig. S2a and Table S2). This validates our selection of geometric surface area instead of Brunauer–Emmett–Teller (BET) specific surface area for the calculation of  $ET(i)$ . **b** Equivalent thickness versus square root of time (UV–Vis spectroscopy data)

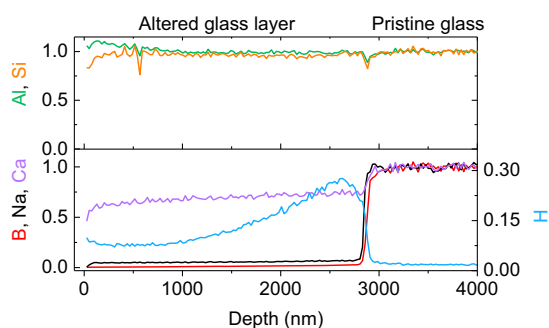


**Fig. 3** ToF-SIMS profiles. ToF-SIMS data obtained from ISG monolith altered for 25 days.  $Si, Al, B, Na,$  and  $Ca$  profiles are normalized to that of  $Zr$  to avoid matrix effects; the resulting data are normalized to that measured in pristine glass to provide quantitative information. The  $H$  profile is not normalized and is only used to locate the alteration front. The Methods section contains more information on data normalization

the end of the experiment.  $Si, Al,$  and  $Zr$  losses are negligible, as shown by the ratios between those network formers; they are relatively similar, within analytical error, in the pristine and altered glass powders.

The glass composition provides some structural information. Boron speciation can be calculated<sup>21</sup> using the network former and network modifier contents of the glass ( $B^{[4]}/(B^{[3]} + B^{[4]}) = 0.44$ ). The number of NBO can be determined from the charge balance obtained from the glass composition<sup>22</sup> (Table 2). For the pristine glass, 4.5% of O atoms in the lattice are NBO. For the altered glass, the structure is globally neutral (Table 2), meaning that all remaining cations such as  $Na$  and  $Ca$  are present as charge compensators rather than as network modifiers. The NBOs within the structure are therefore likely present as hydroxyl groups.

The solution data are consistent with ToF-SIMS profiles (Fig. 3) obtained from monolithic ISG altered for 25 days under similar conditions (90 °C, pH 7, silica-saturated solution), which confirm the near total release of  $B$  and  $Na$  from the alteration layer. The  $Si$  and  $Al$  profiles are flat. The  $Ca$  normalized profile presents a slight decrease from the reaction front to the altered glass layer/solution interface, with a mean retention of  $69 \pm 5\%$  in the alteration layer. This value is similar to that obtained from the direct chemical analysis of both the pristine and altered glasses (see above). The  $H$  profile is not normalized and therefore the profile shape is uncertain and the  $H$  concentration unknown. However, the location of the steep step is consistent with that in the  $B$  profile. These steps, also observed in the  $Na$  and  $Ca$  profiles, are abrupt, with widths of  $\sim 30, \sim 50,$  and  $\sim 80$  nm for  $Na, Ca$  and  $B,$  and  $H,$

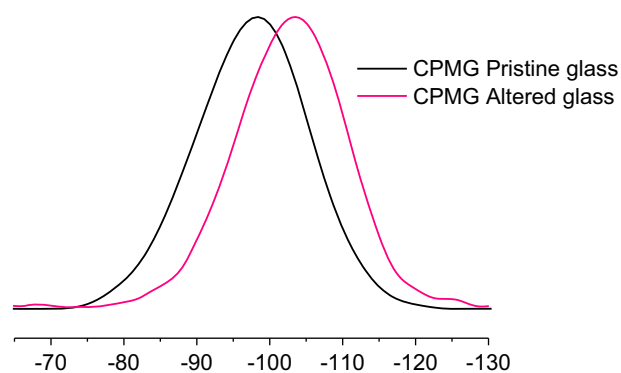
respectively. The presence of the step located at the same depth is consistent with the presence of a dissolution front of mobile glass cations at the pristine/alterated glass interface.<sup>5</sup> All results indicate a homogeneous altered glass network, with some uncertainty regarding  $H$  homogeneity.

#### Structural analysis of the pristine and altered glass

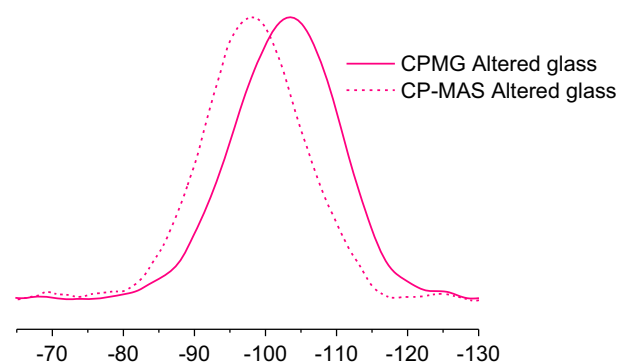
Structural analysis was performed on 3.5–5.5  $\mu m$  pristine and altered glass powders using solid-state NMR spectroscopy, with results shown in Fig. 4. Several isotopes of interest present in ISG were probed, including  $^{29}Si, ^{27}Al, ^{23}Na,$  and  $^{11}B$ . The  $B$  signal in pristine glass was deconvoluted to assess the  $B^{[4]}/(B^{[3]} + B^{[4]})$  ratio (see Supplementary Material Fig. S4a), estimated as  $0.52 \pm 0.02$ . No  $B$  or  $Na$  signals were detected in the altered glass, confirming that both elements are nearly totally leached.

The  $^{29}Si$  magic-angle spinning (MAS) Carr–Purcell–Meiboom–Gill (CPMG) NMR spectra depicted in Fig. 4a show a negative chemical shift  $\delta_{Si}$  between the pristine and altered glass. Higher  $\delta_{Si}$  are usually attributed to higher  $Q^n$  such as  $Q^3$  and  $Q^4$ .<sup>8</sup> While this shift has been attributed to a repolymerization of the silicate network in our previous work with ISG glass altered in the same conditions,<sup>8</sup> it could also be a consequence of  $Si$  second neighbor modification in this case.  $Al, Zr,$  and  $B^{[4]}$  all tend to cause an increase of  $\delta_{Si}$  because of their electronegativity.<sup>14,21,23,24</sup> As seen above,  $B$  release from pristine glass is near total, which could explain the shift to more negative  $\delta_{Si}$ . On the contrary,  $Ca$  tends to cause a decrease of  $\delta_{Si}$  which could be another contribution to the shift observed from pristine to altered glass spectra.<sup>25</sup> No hypothesis can be validated here due to the inability to deconvolute each signal to assess the average  $Q^n$  distribution in each complex material. IR spectrum obtained on both pristine and altered glass and compared to that of amorphous silica show that the structure of the altered sample is more similar to that of amorphous silica than that of pristine glass, highlighting once again the impact of chemical composition variations on the peaks position (see Supplementary Material Fig. S4b). However, like NMR data, these results give no direct information on the difference of polymerization degree between pristine and altered material.

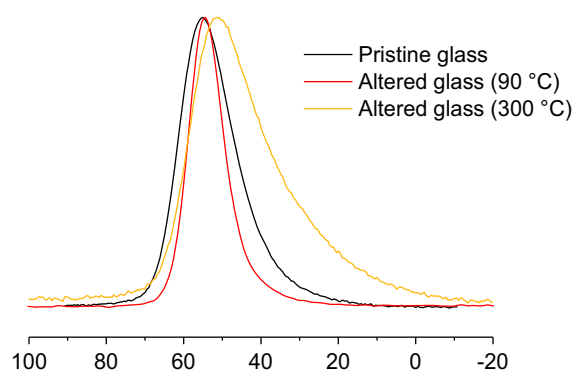
$^1H$ – $^{29}Si$  cross-polarization MAS (CP-MAS) experiments, which rely on the transfer of magnetization from neighboring protons to  $Si$  atoms, are performed on the altered glass powder. This pulse sequence favors the signal of  $Si$  species near protons, such as silanol, and consequently non- $Q^4$  species at lower  $\delta_{Si}$ . The MAS NMR spectrum is centered on a less negative  $\delta_{Si}$  than the signal of CP-MAS, as shown in Fig. 4b. This confirms the presence of silanol groups in the altered glass. When the altered glass is heated at 90 °C, no significant shift of the CP-MAS peak maximum is observed, while at 450 °C, a slight shift is visible (see



(a) Solid NMR -<sup>29</sup>Si chemical shift (ppm)



(b) Solid NMR -<sup>29</sup>Si chemical shift (ppm)



(c) Solid NMR -<sup>27</sup>Al chemical shift (ppm)

**Fig. 4** Solid-state NMR spectroscopy performed on both pristine and altered glass. **a** <sup>29</sup>Si magic-angle spinning (MAS) Carr–Purcell–Meiboom–Gill (CPMG) NMR spectra of the 3.5–5.5 μm pristine and altered glass powders. **b** <sup>29</sup>Si MAS CPMG and cross-polarization (CP) MAS NMR spectra of the altered glass sample. **c** <sup>27</sup>Al MAS NMR spectra of pristine and altered glass samples before and after heating. All spectra are normalized to the same maximum height

Supplementary Material Fig. S4c), indicating a recondensation of silanol groups followed by the release of water.

Solid-state <sup>27</sup>Al MAS NMR spectra are depicted in Fig. 4c. The pristine glass signal is centered at 55 ppm, corresponding to tetrahedral Al compensated mostly by Na.<sup>26</sup> This line shape, typical of a vitreous material, arises from the distribution of isotropic chemical shifts and quadrupolar parameters (see ref. <sup>27</sup>). The peak of the altered glass heated at 90 °C, centered at 54 ppm, is narrower than that of pristine glass. This is highly suggestive of a hydrated local environment of [AlO<sub>4</sub>]<sup>-</sup>, as the presence of water molecules near Al typically narrows the Al signal.<sup>26</sup> All Al species

are susceptible to polarization transfer, as attested by the comparison between the <sup>27</sup>Al MAS and CP-MAS signals (see Supplementary Material Fig. S4d). Heating the altered glass at higher temperatures allows water evaporation. The signal of the altered glass after heating at 300 °C thus shows less proton interference than that of glass heated at lower temperatures (see Supplementary Information Fig. S4e for more data). Significant peak broadening, as well as a slight shift of the peak maximum from 55 to 51 ppm, is observed. Because all Na is leached from the glass and only Ca remains, Ca is assumed to become the charge compensator, as observed previously by Angeli et al.<sup>26</sup> Water compensation of Al at low temperatures cannot be totally ruled out. However, the altered glass structure is globally neutral in charge. It is therefore assumed that Al compensation is mostly ensured by Ca, as otherwise a positively charged structure would be observed.

**Density calculation.** The isovolumetric nature of glass alteration in silica-saturated conditions was investigated using white-light vertical scanning interferometry (VSI). This method allows the measurement of a height step on a flat surface partly covered by a mask to serve as a reference after alteration. The analysis was performed on a monolith altered for 15 days (see Supplementary Material Fig. S5 for more data). A slight swelling of 50 ± 30 nm compared to the original surface was measured. Using the linear regression from Fig. 2b, the thickness of the alteration layer is calculated as ~1800 nm after 15 days, with swelling representing ~3% of the total altered glass thickness. This confirms the absence of silicate network dissolution. The small variation is neglected in the following analysis.

The density of each material was determined using the altered and pristine glass compositions. The density calculated for pristine glass (Table 2) is consistent with experimental measurements.<sup>28</sup> Both models<sup>29,30</sup> used here yield lower densities for the altered glass density than for the pristine glass, consistent with the loss of mobile species at constant volume.

Lastly, both the pristine and altered glass compositions were used to determine the free volume generated by the dissolution of mobile B, Na, and Ca. Ca and Na are considered spherical ions with the volume  $V_{\text{ions}}$  when leached:

$$V_{\text{ions}} = \frac{4\pi r_i^3}{3}, \quad (2)$$

where  $r_i$  is the radius of the ion  $i$ , equal to 1.17 and 1.00 Å for Na and Ca, respectively.<sup>31</sup> The corresponding volumes for Na and Ca are  $6.7 \times 10^{-24}$  and  $4.2 \times 10^{-24}$  cm<sup>3</sup>, respectively. For B, we consider the volumes of both B<sup>[3]</sup> and B<sup>[4]</sup> species, estimated as 29.0 and 52.1 × 10<sup>-24</sup> cm<sup>3</sup>, respectively.<sup>15</sup> The B<sup>[4]</sup>/(B<sup>[3]</sup> + B<sup>[4]</sup>) ratio of 0.52 is determined from the pristine glass <sup>11</sup>B NMR signal (see above). Assuming an isovolumetric alteration, the free volume left after the leaching of mobile elements is ~33.5%. This result can be compared to the free volumes obtained using water quantification and speciation (see above). The free volume in ISG after dissolution was also calculated based on the ISG structure generated from MD simulations by removing the mobile elements (all of B and Na and 30% of Ca) and unbound O. The calculation, based on the solvent-excluded surface<sup>32</sup> implemented in Materials Studio 6.5 (ref. <sup>33</sup>), converged to 30% for a probe radius smaller than 0.1 Å (see Supplementary Material Fig. S1g). This result is in good agreement with the previous estimation, suggesting that the assumption of the quasi-isovolumetric transformation of the pristine glass into a porous and hydrated material is reasonable.

**Pristine and altered glass dissolution rate.** Initial dissolution rate measurements ( $r_0$ ), measured on 4.5–5.5 μm pristine and fully altered glass powder and obtained from the Si concentration, were replicated twice for each sample (Table 2). These rates were measured in extremely dilute conditions and correspond to the

intrinsic resistance of the silicate networks to hydrolysis. The average initial rate measured for pristine ISG approaches 1.24 and  $1.21 \text{ gm}^{-2} \text{ day}^{-1}$  expected at  $\text{pH}_{90^\circ\text{C}}$  7 calculated by Inagaki et al.<sup>34</sup> and Fournier et al.<sup>35</sup>, respectively. The initial dissolution rate of the altered glass is one order of magnitude lower than that of the pristine glass, which could be attributed to a greater polymerization degree of the silicate network in the altered ISG, or to differences in chemical composition.

**Water speciation analysis.** Three types of water species were studied here: molecular water ( $\text{H}_2\text{O}_{\text{mol}}$ ), non-H-bonded hydroxyl species (“free”  $-\text{X}-\text{OH}$ ), and H-bonded hydroxyl species ( $-\text{X}-\text{OH}_{\text{HB}}$ ). Thermogravimetric analyses (TGA) quantifies the total water content of all three species, giving value of 1.2 wt% for pristine glass and 16.5 wt% for altered glass (Table 2). For pristine glass, the water content is assumed to comprise water molecules adsorbed on the particle surfaces. Assuming that this quantity of water molecule adsorbed on the surface is equivalent for pristine and altered glass, this gives an uncertainty of 7% on the global water content. A major water species loss is observed under  $90^\circ\text{C}$  for the altered glass reaching 34% of the global water content.

Applied to the 3.5–5.5- $\mu\text{m}$ -altered glass powder, infrared (IR) spectroscopy showed that only molecular water dehydration

occurred below  $150^\circ\text{C}$ , as the silanol signal at  $\sim 875 \text{ cm}^{-1}$  does not decrease below this temperature. Above  $150^\circ\text{C}$ , silanol species begin to condense. Their contribution to the  $875 \text{ cm}^{-1}$  peak decreases while the Si–O–Si signal at  $800 \text{ cm}^{-1}$  increases significantly (Fig. 5a). The evolutions of the  $\text{H}_2\text{O}_{\text{mol}}$  signal at  $1650 \text{ cm}^{-1}$  (Fig. 5b) indicate that some water within the material is not easily evaporated.

Two methods of direct acquisition (DA) and Hahn Echo (HE) pulse sequence with variable echo delay were used to acquire  $^1\text{H}$  NMR signals from the 3.5–5.5- $\mu\text{m}$ -altered glass powder. When heating the sample from 25 to  $150^\circ\text{C}$ , decreases of the DA  $^1\text{H}$  NMR signal areas at  $\sim 7.1$  and  $\sim 5.1$  ppm are visible (Fig. 5c) (spectra are normalized to the same sample weight). This is followed by a displacement of the signal toward more negative chemical shift values when the sample is heated from 150 to  $450^\circ\text{C}$ . The main contributions remaining are those at  $\sim 3.6$  ( $300^\circ\text{C}$ ) and  $\sim 2.2$  ppm ( $450^\circ\text{C}$ ). The HE pulse sequence allows better species distinction based on the  $^1\text{H}-^1\text{H}$  dipolar couplings, approximately equivalent to the local proton density, of the different species, as stronger dipolar couplings imply shorter decays in echo signals.<sup>26</sup> Typically, water molecule signals show shorter decays. Therefore, HE  $^1\text{H}$  NMR was used to distinguish the various contributions to the DA  $^1\text{H}$  NMR signal. The results, displayed in Fig. 5d, are obtained from

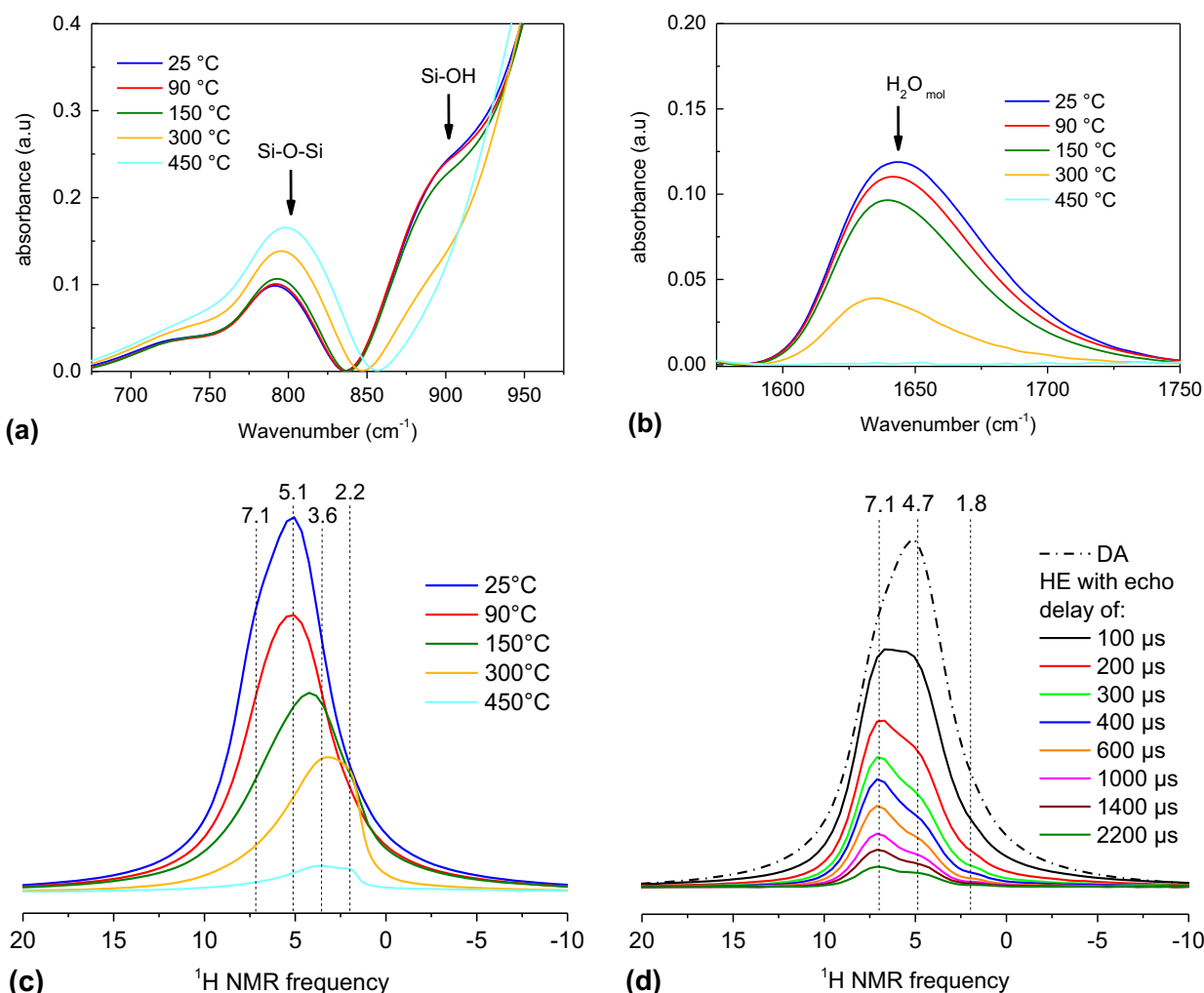


**Fig. 5** IR and  $^1\text{H}$  MAS NMR spectroscopy performed on the altered glass. **a, b** IR spectra of the 3.5–5.5- $\mu\text{m}$ -altered glass powder before and after heat treatment. All spectra are normalized to the same maximum height. **c**  $^1\text{H}$  MAS NMR spectra of the 3.5–5.5- $\mu\text{m}$ -altered glass powder before and after heat treatments at different temperatures. Spectra are normalized to the sample mass. **d**  $^1\text{H}$  MAS NMR signal obtained by DA and using an HE pulse sequence with varying echo delays on the altered sample at ambient temperature (see Supplementary Material Fig. S6a for results from heated samples)

an unheated sample (see Supplementary Material Fig. S6 for data obtained from heated samples). A broad contribution centered at 4.7 ppm, rather than 5.1 ppm, is observed. It decreases in intensity when the sample is heated at low temperatures (90–150 °C). This contribution can therefore be attributed to physisorbed water. A second signal centered at 7.1 ppm is attributed to H-bonded hydroxyl species. This contribution decreases in intensity and shifts to lower values (~3.8 to 3.6 ppm) when the sample is heated, as fewer H bonds can form when water molecules are released. Finally, a third contribution appears at ~1.8 ppm. This contribution is intensified for samples heated to higher temperatures (300–450 °C); it is therefore attributed to non-H-bonded (i.e., isolated) hydroxyls.

## DISCUSSION

### Pristine and altered glass structures

The ISG structure was simulated and the model was validated by experimental observation. Cation coordination numbers from MD simulations (Table 1) are in good agreement with previous simulation results.<sup>36,37</sup> These results are also consistent with experimental data.<sup>38,39</sup> The  $B^{[4]}/(B^{[3]} + B^{[4]})$  ratio determined from the MD simulation (0.59) is somewhat higher but still relatively near the experimental values ( $0.52 \pm 0.02$  from NMR and 0.44 from glass composition) as well as a value obtained previously (0.49 (ref. 7)). The latter formula excludes Ca, which might explain the slight decrease in the calculated value relative to the experimental one. The Si  $Q^n$  distribution could not be directly obtained experimentally, because the chemical shift dispersion caused by second-nearest neighbors (mainly Si–O–Al and Si–O–B, and Si–O–Zr to a smaller extent) is superimposed on the standard  $Q^n$  dispersion observed in pure silicates. Nonetheless,  $Q^n$  repartition obtained from the MD simulation was partly validated by the similarity between the number of NBO simulated using Si  $Q^n$  (3.7%) and that calculated from the glass composition (4.5%).<sup>21</sup>

Zr is mostly six-coordinated, consistent with X-ray absorption near edge structure and extended X-ray absorption fine structure studies of similar glasses,<sup>40</sup> and appears to be preferentially charge-compensated by Ca in our simulations. Al is compensated by both Ca and Na in the MD simulation. Na and Ca display the same normalized probability of presence near Al sites (Fig. 1e). Considering the Na and Ca contents of the glass, approximately twice as many Al–Na sites as Al–Ca are present in ISG, exceeding the level suggested by NMR data. The <sup>27</sup>Al signal shows that, in pristine ISG, Al is mostly compensated by Na.<sup>26</sup> Potential sets with rigid charges are too simple in the description of electrostatic interactions to describe Al compensation properly.

Finally, ring size distributions suggest that B is important as a crosslinking element within the aluminosilicate network. This is supported by the higher polyhedral connectivity percentages of  $[BO_{3/4}]$ – $[SiO_4]$ . This structural feature must significantly affect glass corrosion. Because B is preferentially dissolved during glass alteration relative to the other glass formers, a very fragmented nanoporous network structure remains, mostly comprising  $[SiO_4]$  and  $[AlO_4]$  units that can re-polymerize.

Indeed, when using “soft” alteration conditions (near neutral pH, silica saturated solution), B and Na release from ISG are initially fast and then decreasing but silicate network hydrolysis remains very low, as revealed by solid chemical analysis, solution analysis data, and ToF-SIMS profiles. <sup>29</sup>Si NMR results show negative shifts  $\delta_{Si}$  between the pristine and altered glass. This shift, already observed by Gin et al.,<sup>8</sup> was attributed at first to a reorganization of the silicate network that increases the polymerization degree, as the  $Q^4$  and  $Q^3$  contributions have lower isotropic chemical shifts than those of  $Q^2$  and  $Q^1$ .<sup>26,41</sup> However, oxygen repartition as BO and NBO in pristine and altered structures was determined (Table 2) (refer to Supplementary Material part 8 for more information). The

results obtained before and after boron release in pristine glass are consistent with the observation stated above regarding B connectivity from the simulated glass structure. B release creates a fragmented structure with a lot of NBO. This structure then reorganizes into a more thermodynamically stable state, passing from 43.8 to 22% of NBO (Table 2). These NBO remains in the altered glass as silanol, as demonstrated by the difference in the chemical shift position from CP-MAS to CPMG pulsed <sup>29</sup>Si signals. While there is a non-negligible repolymerization of the network after mobile elements departure, the altered glass structure is not more polymerized than the pristine glass structure. The differences observed between initial dissolution rates can therefore be explained by chemical composition changes. B–O–B and B–O–Si bridges are easier to hydrolyze than Si–O–Si, as their hydrolysis activation energy are lower.<sup>42</sup> The altered glass structure is nearly devoid of B; its remaining bonds are expected to be more difficult to hydrolyze than that of pristine glass containing 9.6 At% of B. The presence of water may also decrease the internal energy of the material by relaxing strain accumulated during glass quenching.<sup>11</sup>

During alteration, it was seen that B and Na releases were congruent, but Ca exhibited a different behavior, with some Ca remaining in the altered layer to ensure the charge compensation of  $AlO_4^-$  and  $ZrO_6^{2-}$  units. MAS NMR <sup>27</sup>Al data support this hypothesis. No change in coordination, which would be indicated by the formation of  $AlO_5$  or  $AlO_6$  units, is observed. The significant broadening and the slight shift of the peak maximum from 55 to 51 ppm indicate a change of the charge compensator species. Angeli et al.<sup>26</sup> showed that, while the isotropic chemical shift  $\delta_{iso}$  remains constant when an  $[AlO_4]^-$  unit is compensated by Ca rather than by Na, the distribution of the quadrupolar interaction shift is broadened dramatically.<sup>43</sup> The signal obtained here is therefore consistent with that of the Al tetrahedral charge compensation by Ca cations.

Finally, B release is well correlated with the square root of time (Fig. 2b). Assuming that this behavior can be modeled by Fick's equations, the apparent B diffusion coefficient,  $D_B^{Fick}$  of  $\sim 10^{-18} m^2 s^{-1}$  was derived. Note that this calculation does not indicate that B diffusion is the rate-limiting step, as B release may be caused by another rate-limiting process. This apparent diffusivity is in the same range as apparent diffusion coefficients found at 90 °C and pH 8.7 for simple nuclear glasses ( $D \sim 10^{-19} m^2 s^{-1}$  in pure water and  $D \sim 10^{-21} m^2 s^{-1}$  in Si-saturated solution<sup>44</sup>). Importantly, these values of diffusivity are 10 to 12 orders of magnitude lower than the diffusion coefficient of aqueous species in a bulk solution ( $D \sim 10^{-9} m^2 s^{-1}$ ),<sup>45</sup> indicating that they refer to solid-state diffusion within the nanoporous layer.<sup>46</sup> Moreover, abrupt steps such as those observed in the ToF-SIMS profiles shown in Fig. 3 are consistent with the presence of a dissolution front that progresses into the pristine material at a rate controlled by the flux of water molecules through the growing alteration layer, as suggested in a previous work.<sup>5,8</sup> Therefore, water speciation must be studied further.

### Water speciation and porosity analysis

Several water species can be found in the studied altered glass. Molecular water  $H_2O_{mol}$ , also called physisorbed water, can be adsorbed onto grain surfaces or confined within pores. Hydroxyl groups, such as silanol –Si–OH, are known as chemisorbed water.<sup>47</sup> They can exist as “free” species that do not form H bonds, or as H-bonded species called –X–OH<sub>HB</sub> in this study.

The TGA and NMR data are well correlated, as shown in Fig. 6a. This curve could be used for calibration in further studies, as TGA is a destructive testing method and thus may be prohibited when the sample quantity is limited. Such calibration models have been developed in other fields such as glass manufacturing<sup>48,49</sup> and geochemistry<sup>50–53</sup> using TGA and IR or Raman spectroscopy data.

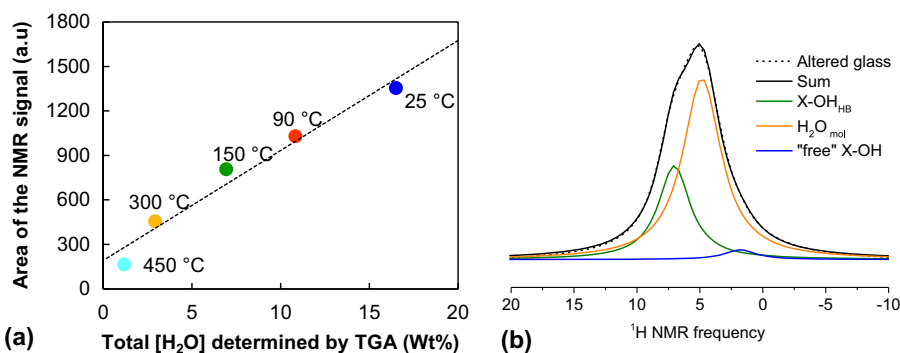


**Fig. 6** TGA and  $^1\text{H}$  NMR data comparison. **a**  $^1\text{H}$  NMR signal areas determined at various temperatures (25, 90, 150, 300, and 450 °C); these results are compared to the total water quantity ( $\text{H}_2\text{O}_{\text{mol}}$  + hydroxyl species) found by TGA at each temperature. They are well correlated. **b** Deconvoluted  $^1\text{H}$  NMR signal (at 25 °C)

Unfortunately, these models are highly dependent on the glass composition and cannot be translated to nuclear glass alteration studies. Because ISG has recently become a reference for nuclear glass alteration studies,<sup>1</sup> the development of such a calibration model is worthwhile.

IR spectroscopy results showed that no silanol dehydration occurred below 150 °C, meaning that the 58% of water species dehydrated below 150 °C (see Table 2) were  $\text{H}_2\text{O}_{\text{mol}}$ . The remaining 42% of water species are residual  $\text{H}_2\text{O}_{\text{mol}}$ ,  $-\text{X}-\text{OH}_{\text{HB}}$ , and “free”  $-\text{X}-\text{OH}$ .  $^1\text{H}$  NMR spectroscopy results allow more detailed water species repartition. The 1.8 ppm contribution corresponds to isolated hydroxyls, i.e., those not forming H bonds.<sup>26,54,55</sup> The broad signal at  $\sim 4.7$  ppm is commonly attributed to protons in physisorbed water molecules.<sup>26,54,56</sup> The decrease in signal intensity when the sample is heated below 150 °C is then consistent with  $\text{H}_2\text{O}_{\text{mol}}$  evaporation. The contribution at 7.1 ppm, observed only at low temperature, corresponds to the mean isotropic chemical shift of hydrogenated hydroxyl species.<sup>54,55</sup> This contribution decreases at lower temperatures (90–150 °C), and shifts lower ( $\sim 3.6$  ppm) at higher temperatures (300–450 °C). These changes indicate that the signal mostly arises from hydroxyl species strongly bonded to water molecules, which yields hydroxyls weakly bonded to O in the silicate network (contribution at 3.6 ppm) as well as non-bonded hydroxyl (contribution at 1.8 ppm).

Using the three contributions detailed above (1.8, 4.7, and 7.1 ppm), the 25 °C signal was deconvoluted (see Fig. 6b), allowing the H species repartition detailed in Table 2. Combining TGA, NMR, and chemical analysis data, O species repartition as bridging-oxygen  $\text{O}_{\text{BO}}$ , non-bridging-oxygen (hydroxyl species)  $\text{O}_{\text{NBO}}$ , and water-oxygen  $\text{O}_{\text{H}_2\text{O}}$ , was determined as well (refer to Supplementary Material part 7–8 for O speciation calculation).

Based on the water speciation and on TGA data, the surface area and volume of the porosity as well as the average pore size can be determined (Table 2) (refer to Supplementary Material part 7 for more information on the way those parameters were calculated). The porosity obtained from the release of mobile elements (33.5%) is between the values found for the effective and total volumes. Depending on the chosen “free” volume and on the heat treatment, values of mean pore diameter  $d$  vary between 0.9 and 1.9 nm. While this calculation using a single pore type yields a rough estimation of mean pore size, it gives a very small value below the detection limits of typical analytical techniques, such as gas physisorption, small-angle X-rays scattering, and thermoporometry. The results are consistent with previous tracing experiments with  $\text{D}_2\text{O}$  and dyes, showing that this type of altered layer acts as a molecular sieve with a cutoff of  $\sim 1$  nm.<sup>8</sup> Although the pore network is not fully characterized, these results strongly suggest that water molecules are confined

in small pores; the nature of their interactions with pore walls and their microscopic and macroscopic diffusion remain to be determined.

### Concluding remarks

- The simulated structure of ISG was validated by experimental data, and therefore provided previously unknown structural information such as  $Q^n$  repartition. The ISG structure is now characterized and can be used for further alteration or irradiation studies.
- The experimental results of this study provide a better understanding of both pristine and altered ISG structures. The altered layer obtained in silica saturation conditions is formed by in situ reorganization of the aluminosilicate network after the release of mobile species. This reorganization allows the relaxation of strain accumulated during glass quenching, entailing a decrease in the network’s internal energy. The resulting material has greater resistance to hydrolysis than that of the pristine glass.
- Combining multiple analytical techniques, the departure of mobile species is shown to leave a free nanoporous volume. The calculated mean pore size is  $\sim 1$  nm in diameter. The pore volume is filled with water molecules as well as free and H-bonded hydroxyl species, which were quantified. Some questions remain regarding water dynamics inside such a nanoporous material. The exchange of water species inside the altered glass structure and the rate of exchange must be determined. This could provide new information on the glass corrosion rate-limiting mechanism.

## METHODS

### MD simulations

MD simulations were conducted with the DL\_POLY simulation package.<sup>57</sup> In MD simulations, the empirical potential is critical in generating realistic structures and descriptions of glass properties. Here, a partial-charge pairwise potential with a combination of long-range Columbic terms and short-range Buckingham terms is used; it has shown high transferability and computational efficiency in modeling multicomponent glasses.<sup>17</sup> The formula of the Buckingham term is shown in Eq. 3:

$$V_{ij} = A_{ij} \exp(-r_{ij}/\rho_{ij}) - C_{ij}/r_{ij}^6, \quad (3)$$

where  $i$  and  $j$  are the elements of the  $i$ - $j$  pair,  $A_{ij}$ ,  $\rho_{ij}$ , and  $C_{ij}$  are the empirical parameters for pair  $i$ - $j$ , and  $r_{ij}$  is the interatomic distance of the  $i$ - $j$  pair. In

order to solve the high-temperature issue, a repulsion term:

$$V_{ij}(r_{ij}) = \frac{B_{ij}}{r_{ij}^{n_{ij}}} + D_{ij}r_{ij}^2 \quad (4)$$

is added to correct it. The  $B_{ij}$ ,  $n_{ij}$ , and  $D_{ij}$  values are obtained by maintaining continuity in the potential, force, and first derivative of the force curves at the point where the second derivative of the force approaches 0. The parameters for O–O, Si–O, Al–O, Na–O, Ca–O, and Zr–O pairs were previously published.<sup>17</sup> The B-related potentials were recently developed, consisting of composition-dependent parameters fitted with structures such as solid-state NMR results and properties. The atomic charges of the atoms and the Buckingham parameters  $A_{ij}$ ,  $\rho_{ij}$ , and  $C_{ij}$  (Eq. 3) used in our simulations can be found in Supplementary Material Table S9.

The ISG bulk structure with a system size of 24,000 atoms was simulated through a melting and quenching process. The initial structures were energy-minimized at 0 K and then relaxed at 300 K through a canonical process (with constant atom number, constant volume, and constant temperature (NVT) ensemble). Afterward, the systems were melted at 6000 K, equilibrated at 5000 K, and then cooled to 300 K at 5 K ps<sup>-1</sup> using the NVT ensemble. After the melting–quenching process, the structures were equilibrated at 300 K under an isothermal–isobaric process (with constant atom number, constant pressure, and constant temperature (NPT) ensemble) combined with an NVT process. Structural analyses, such as the PDFs and  $Q^n$  speciation statistics, were achieved from the configurations of the simulated glasses at 300 K.

### Leaching experiments

All experiments were performed on an ISG batch prepared by MoSci Corporation (Rolla, MO, USA). Refer to Gin et al.<sup>8</sup> for more information on glass preparation. The glass was crushed into powder, which was sieved before washing in acetone and ethanol to remove fine particles. Leaching experiments were conducted on the fraction with particles of 20–40 μm in size for the alteration kinetic study, and on the 3.5–5.5 μm size fraction to obtain a totally altered glass powder for solid characterization. SEM was performed on the 3.5–5.5-μm-sized glass powder to verify the size of the powder particles (see Supplementary Material Fig. S10); such small particle sizes are difficult to obtain.

All experiments were prepared in perfluoroalkoxy reactors using 18.2 MΩ cm deionized water (DIW) initially saturated with respect to amorphous silica ( $C_0(\text{Si}) = 143 \text{ mg L}^{-1}$  at pH<sub>90°C</sub> 7). SiO<sub>2</sub> was introduced under agitation at 90 °C until total dissolution occurred. In the alteration conditions selected for this study, glass alteration kinetics are expected to be the same whatever the geometry of the experiment and the surface-area-to-solution-volume ( $S/V$ ). They only depend on time.

During the experiment, the pH was maintained at  $7.0 \pm 0.5$  by adding small quantities of a 0.5 N nitric acid solution. The solution was regularly sampled over time. The samples were filtered (0.45 μm cutoff) and analyzed by spectrophotometry (Cary® 50 Scan UV-Vis spectrophotometer for B concentration, with a method analogous to DIN 38405-17) and inductively coupled plasma atomic emission spectroscopy (ICP-AES; Thermo Scientific iCAP™ 6000 Series).

**Alteration kinetic study.** Specimens of 200 mg of the 20–40 μm glass powder and two monoliths measuring  $0.5 \times 0.5 \times 0.2 \text{ cm}$ , polished to 1 μm on the two largest sides, were introduced to 0.5 L of silica-saturated solution at 90 °C ( $S/V = 34 \text{ m}^{-1}$  with  $S_{\text{geo}} = 0.08 \text{ m}^2 \text{ g}^{-1}$ ). The first monolith was withdrawn after 25 days and the second after 134 days. Various parameters were derived from the solution analysis data, such as the altered glass percentage and equivalent thickness.

The glass alteration percentage AG% could be assessed at any time  $t$  from the B concentration [B] in solution, using the following equation:

$$\text{AG}\% = \frac{[\text{B}]^t \cdot V^t + \sum_{i=1}^{t-1} [\text{B}]^i \cdot V_i^{\text{sample}}}{m_{\text{B in the glass}}}, \quad (5)$$

where  $V^t$  is the total volume of the reactor at a time  $t$ ,  $V_i^{\text{sample}}$  is the volume of the sample  $i$ , and  $m_{\text{B in the glass}}$  is the total mass of B leached from the glass powder. This formula considers solution sampling over time. The equivalent thickness (μm), which assumes that the particles are shrinking over time, can be calculated using AG%:

$$\text{ET}(\text{B})^t = \frac{3}{S_{\text{geo}} \cdot \rho} \left[ 1 - \left( \frac{100 - \text{AG}\%}{100} \right)^{\frac{1}{3}} \right], \quad (6)$$

where  $\rho$  is the pristine glass density. We use the geometric surface  $S_{\text{geo}}$  here, rather than the specific surface area measured by gas adsorption and

the application of the Brunauer–Emmett–Teller (BET) model. This surface area is calculated using the following formula:

$$\frac{6/\rho}{\sqrt{3.5 \times 10^{-6} \text{ m} \times 5.5 \times 10^{-6} \text{ m}}}, \quad (7)$$

where  $\rho$  is the pristine glass density. Alteration rates (in nm day<sup>-1</sup>) are easily extracted from the equivalent thickness:

$$r = \frac{d(\text{ET}(\text{B}))}{dt} \quad (8)$$

using a moving average from three consecutive points.

**Glass preparation for total alteration.** A sample of 500 mg of 3.5–5.5 μm glass powder was introduced to 1 L of silica-saturated solution at 90 °C ( $S/V = 274 \text{ m}^{-1}$  with  $S_{\text{geo}} = 0.55 \text{ m}^2 \text{ g}^{-1}$ ). The solution was regularly checked over time until total B release from the glass had occurred. The solution was then filtered using a Büchner funnel, and the altered glass powder was dried for 24 h at 50 °C and stored in a desiccator.

**Initial dissolution rate measurement.** The initial dissolution rates of both pristine and altered glass were measured by static alteration measurements at pH<sub>90°C</sub> 7 in DIW. Contrary to the previous experiments no silica was added in the onset solution. Two measurements were done on 3.5–5.5 μm pristine and altered glass powders ( $S/V = 0.18 \text{ cm}^{-1}$ ) to ensure the repeatability of the experiment. The Si concentration was monitored over time by spectrophotometry and ICP-AES. For more extensive details on the procedure, please refer to Fournier et al.<sup>58</sup>

**Solid analysis.** Solid analyses were performed on the 3.5–5.5-μm-altered glass powder and on monoliths.

**Chemical analysis.** A small fraction of altered 3.5–5.5 μm glass powder was dissolved in an acid solution (10 HCl + 5 HNO<sub>3</sub> + 4 HF). The resulting solution was analyzed by ICP-AES (Thermo Scientific iCAP™ 6000 Series) to quantify Si, B, Na, Al, Ca, Zr, and K in the altered glass. Two analyses were conducted for repeatability. O in the altered glass was considered using the following equation:

$$O_{\text{altered glass}} = \sum O_i \text{ pristine glass} \cdot \frac{[i]_{\text{altered glass}}}{[i]_{\text{pristine glass}}}, \quad (9)$$

where  $i = \text{Si, B, Na, Al, Ca, and Zr}$ ,  $O_i \text{ pristine glass}$  being therefore the number of O atoms associated with each element in the pristine glass.

**Density calculation.** The densities of both the pristine and altered glasses were assessed using a model developed by Fluegel<sup>29</sup> for calculating the room-temperature glass density using its composition. The model does not consider water within the sample. Another model, developed by Iacovino,<sup>30</sup> which considers water, was also used for the altered glass density calculation, but this could not be applied to the pristine glass as the model did not consider B.

**Depth profiling analysis.** The monolith withdrawn after 25 days was analyzed using ToF-SIMS (IONTOF TOF 5). An O ion beam was set at 2 keV and 510 nA and used for surface abrasion (200 × 200 μm). Actual analysis was provided by a Bi ion sputtering beam (25 keV, 2 pA, 30 × 30 μm) followed by ToF investigation of secondary ions extracted from the monolith. The surface was neutralized during analysis by a low-energy electron flux (<20 eV). Measuring the depth of the final crater allowed elemental profile depth calibration.

Si, Al, B, Na, and Ca profiles were then normalized to that of Zr to avoid matrix effects. Zr was chosen as it is not leached in solution during the experiment.<sup>59</sup> The resulting data were normalized to the mean measured in pristine glass to extract quantitative information. All of this was done using the following formula:

$$C(i) = \frac{[1/\text{Zr}]}{[1/\text{Zr}]_{\text{pristine glass}}} \quad (10)$$

with  $i = \text{Si, Al, B, Na, and Ca}$ . The H profile was not normalized, and was thus only used to evaluate the position of the alteration front.

**White-light VSI.** In order to assess the volume change during glass alteration in Si-saturated solution, the surface of a glass monolith was partially coated using room-temperature vulcanization (RTV) silicone.<sup>60</sup> The RTV silicone held at pH<sub>90°C</sub> 7 was checked prior to the experiment. The

monolith was then altered for 15 days in conditions similar to those described above. The silicon RTV coating was removed and the sample surface was analyzed by VSI (FOGAL nanotech, magnification 10). The difference between the mean height values of the coated and uncoated surfaces was measured. The uncertainty was determined from the height variations of both sections.<sup>60</sup>

**Thermogravimetric analysis.** TGA analyses were performed on a Seratum TG-DSC 92–16.18, under a flow of Ar in an Al<sub>2</sub>O<sub>3</sub> crucible. Both 3.5–5.5 μm pristine and altered glass powders were analyzed (~70 mg each). For the pristine glass, a typical heating ramp of 10 °C min<sup>-1</sup> was used between room temperature and 1200 °C. For the altered sample, an increased rate (30 °C min<sup>-1</sup>) was used to attain specific temperatures of 90, 150, 300, and 450 °C, with 2-h plateaus at each temperature. A last heating ramp of 10 °C min<sup>-1</sup> was then performed to reach 1200 °C.

**Fourier-transform infrared spectroscopy.** Pristine and altered glass powders were analyzed using a Fourier-transform infrared spectrometer (Bruker VERTEX 70) in transmission mode, equipped with DTGS/KBr detector elements. Spectra were recorded between 400 and 4000 cm<sup>-1</sup>. The 3.5–5.5-μm-altered glass powder was crushed with KBr, which is transparent in the domain of interest, to form a pellet (2/100 ratio). A pure KBr pellet was used as a reference, and a 2 cm<sup>-1</sup> resolution was selected for 1000 acquisitions to obtain a good signal-to-noise ratio. All baseline subtractions and signal normalizations were performed using Fityk 0.9.8 software. The silicate network band attribution was based on the work of Aguiar et al.,<sup>61</sup> while water band attribution was based on the work of Davis and Tomozawa.<sup>62</sup>

**NMR spectroscopy.** <sup>1</sup>H and <sup>29</sup>Si MAS NMR analyses were performed on a Bruker Avance WB 300 MHz spectrometer (magnetic field 7.05 T). A Bruker 4-mm (external diameter of ZrO<sub>2</sub> rotor) CP-MAS probe was used at a sample rotation frequency of 10 kHz. The average sample mass was 90 mg. <sup>29</sup>Si/<sup>1</sup>H CP-MAS NMR spectra were collected on both 3.5–5.5 μm pristine and altered glass powders using contact times ranging from 2 to 8 ms. <sup>29</sup>Si MAS NMR spectra were also acquired, using the CPMG pulse sequence<sup>63</sup> with a recycle delay of 2 s. As most proton species relax quickly, this delay was satisfactory (see Supplementary Material Fig. S6b and c for more information on proton relaxation).

<sup>1</sup>H MAS NMR signals were obtained from the altered ISG by DA and using an HE pulse sequence with varying rotor-synchronized echo delays ranging from 100 to 80000 μs. <sup>1</sup>H NMR signal deconvolution was completed using the Dmfit program,<sup>64</sup> considering a mixed Gaussian/Lorentzian model. Using the HE sequence data, the position of each contribution was fixed, and the width and amplitude were left free. Automatic optimization was run until reaching convergence.

<sup>11</sup>B and <sup>27</sup>Al MAS NMR spectra were collected on a Bruker Avance II 500WB spectrometer (magnetic field 11.72 T), using a Bruker 4 mm CP-MAS probe at a spinning frequency of 12,500 Hz.

<sup>11</sup>B MAS NMR data were acquired from the pristine ISG, as no signal was detected from the altered sample. The B<sup>(3)</sup>/B<sup>(4)</sup> ratio was extracted from the resulting pristine glass signal by a standard deconvolution procedure.<sup>6</sup>

## Data availability

The data that support the findings of this study are available from the corresponding author upon reasonable request.

## ACKNOWLEDGEMENTS

The authors are grateful to Géraldine Parisot (CEA), Valentine Laporte (CEA), Laurent Dupuy (Biophy Research), Jennifer Renard (CEA), and Jean-Pierre Mestre (CEA) for technical support and scientific input. This work was supported as part of the Center for Performance and Design of Nuclear Waste Forms and Containers, an Energy Frontier Research Center funded by the U.S. Department of Energy, Office of Science, Basic Energy Sciences under Award # DE-SC0016584.

## AUTHOR CONTRIBUTIONS

S.G. supervised the study. M.C. was responsible for experimental analysis and wrote the paper. M.F. and P.F. were involved in data interpretation. T.C., M.M., and M.C. performed the solid-state NMR study. L.D., M.R., and J.D. were in charge of MD simulations. All the authors helped on paper editing.

## ADDITIONAL INFORMATION

**Supplementary information** accompanies the paper on the *npj Materials Degradation* website (<https://doi.org/10.1038/s41529-017-0025-y>).

**Competing interests:** The authors declare no competing financial interests.

**Publisher's note:** Springer Nature remains neutral with regard to jurisdictional claims in published maps and institutional affiliations.

## REFERENCES

1. Gin, S. et al. An international initiative on long-term behavior of high-level nuclear waste glass. *Mater. Today* **16**, 243–248 (2013).
2. Grambow, B. Nuclear waste glasses—how durable? *Elements* **2**, 357–364 (2006).
3. Vienna, J. D., Ryan, J. V., Gin, S. & Inagaki, Y. Current understanding and remaining challenges in modeling long-term degradation of borosilicate nuclear waste glasses. *Int. J. Appl. Glass Sci.* **4**, 283–294 (2013).
4. Jantzen, C. M., Brown, K. G. & Pickett, J. B. Durable glass for thousands of years. *Int. J. Appl. Glass Sci.* **1**, 38–62 (2010).
5. Gin, S. et al. Atom-probe tomography, TEM and ToF-SIMS study of borosilicate glass alteration rim: a multiscale approach to investigating rate-limiting mechanisms. *Geochim. Cosmochim. Acta* **202**, 57–76 (2017).
6. Charpentier, T. et al. Self-healing capacity of nuclear glass observed by NMR spectroscopy. *Sci. Rep.* **6**, 25499 (2016).
7. Mendoza, C. et al. Oxide glass structure evolution under swift heavy ion irradiation. *Nucl. Instrum. Methods Phys. Res., Sect. B* **325**, 54–65 (2014).
8. Gin, S. et al. Origin and consequences of silicate glass passivation by surface layers. *Nat. Commun.* **6**, 1–8 (2015).
9. Gin, S. et al. The fate of silicon during glass corrosion under alkaline conditions: a mechanistic and kinetic study with the International Simple Glass. *Geochim. Cosmochim. Acta* **151**, 68–85 (2015).
10. Neill, L. et al. Various effects of magnetite on international simple glass (ISG) dissolution: implications for the long-term durability of nuclear glasses. *NPJ Mater. Degrad.* **1**, 1–11 (2017).
11. Amma, S.-i., Luo, J., Kim, S. H. & Pantano, C. G. Effects of fictive temperature on the leaching of soda lime silica glass surfaces. *J. Am. Ceram. Soc.* **100**, 1424–1431 (2017).
12. Cormier, L., Ghalib, L., Ghaleb, D. & Calas, G. Short-range and medium-range structural order around cations in glasses: a multidisciplinary approach. *C. R. Acad. Sci. Paris IV* **2**, 249–262 (2001).
13. Delaye, J. M. Modeling of multicomponent glasses: a review. *Curr. Opin. Solid State Mater. Sci.* **5**, 451–454 (2001).
14. Soleilhavoup, A., Delaye, J. M., Angeli, F., Caurant, D. & Charpentier, T. Contribution of first-principles calculations to multinuclear NMR analysis of borosilicate glasses. *Magn. Reson. Chem.* **48**, S159–170 (2010).
15. Barlet, M., Kerrache, A., Delaye, J.-M. & Rountree, C. L. SiO<sub>2</sub>–Na<sub>2</sub>O–B<sub>2</sub>O<sub>3</sub> density: a comparison of experiments, simulations, and theory. *J. Non Cryst. Solids* **382**, 32–44 (2013).
16. Kieu, L.-H., Delaye, J.-M., Cormier, L. & Stolz, C. Development of empirical potentials for sodium borosilicate glass systems. *J. Non Cryst. Solids* **357**, 3313–3321 (2011).
17. Du, J. Challenges in molecular dynamics simulations of multicomponent oxide glasses. First-Principles modeling of binary chalcogenides: Recent accomplishments and new achievements. **215**, 157–180 (2015).
18. Deng, L. & Du, J. Development of effective empirical potentials for molecular dynamics simulations of the structures and properties of borosilicate glasses. *J. Non Cryst. Solids* **453**, 177–194 (2016).
19. Gin, S. et al. The controversial role of inter-diffusion in glass alteration. *Chem. Geol.* **440**, 115–123 (2016).
20. Ferrand, K., Abdelouas, A. & Grambow, B. Water diffusion in the simulated French nuclear waste glass SON 68 contacting silica rich solutions: experimental and modeling. *J. Nucl. Mater.* **355**, 54–67 (2006).
21. Angeli, F., Charpentier, T., De Ligny, D. & Cailleteau, C. Boron speciation in soda-lime borosilicate glasses containing zirconium. *J. Am. Ceram. Soc.* **93**, 2693–2704 (2010).
22. Angeli, F. et al. Influence of lanthanum on borosilicate glass structure: a multinuclear MAS and MQMAS NMR investigation. *J. Non Cryst. Solids* **376**, 189–198 (2013).
23. Engelhardt, G. & Michel, D. *High Resolution Solid State NMR of Silicates and Zeolites* (John Wiley & Sons, Chichester, New York, Brisbane, Toronto, Singapore, 1987).
24. Lapina, O. B., Khabibulin, D. F. & Terskikh, V. V. Multinuclear NMR study of silica fiberglass modified with zirconia. *Solid State Nucl. Magn. Reson.* **39**, 47–57 (2011).
25. Schneider, J. et al. Qn distribution in stoichiometric silicate glasses: thermodynamic calculations and <sup>29</sup>Si high resolution NMR measurements. *J. Non Cryst. Solids* **325**, 164–178 (2003).

26. Angeli, F., Gaillard, M., Jollivet, P. & Charpentier, T. Influence of glass composition and alteration solution on leached silicate glass structure: a solid-state NMR investigation. *Geochim. Cosmochim. Acta* **70**, 2577–2590 (2006).
27. Angeli, F., Gaillard, M., Jollivet, P. & Charpentier, T. Contribution of  $^{43}\text{Ca}$  MAS NMR for probing the structural configuration of calcium in glass. *Chem. Phys. Lett.* **440**, 324–328 (2007).
28. Gin, S., Beaudoux, X., Angeli, F., Jegou, C. & Godon, N. Effect of composition on the short-term and long-term dissolution rates of ten glasses of increasing complexity from 3 to 30 oxides. *J. Non Cryst. Solids* **358**, 2559–2570 (2012).
29. Fluegel, A. Global model for calculating room-temperature glass density from the composition. *J. Am. Ceram. Soc.* **90**, 2622–2625 (2007).
30. Iacovino, K. *Glass Density Calc* v3.2. <http://www.kaylaiacovino.com/tools-for-petrologists/> (2017).
31. Jollivet, P. et al. Effect of clayey groundwater on the dissolution rate of the simulated nuclear waste glass SON68. *J. Nucl. Mater.* **420**, 508–518 (2012).
32. Connolly, M. L. Analytical molecular surface calculation. *J. Appl. Crystallogr.* **16**, 548–558 (1983).
33. Accelrys Software Inc. Discovery Studio Modeling Environment, Release 7.0 (Accelrys Software Inc., San Diego, 2007).
34. Inagaki, Y., Kikunaga, T., Idemitsu, K. & Arima, T. Initial dissolution rate of the international simple glass as a function of pH and temperature measured using microchannel flow-through test method. *Int. J. Appl. Glass Sci.* **4**, 317–327 (2013).
35. Fournier, M., Frugier, P., Gin, S. Resumption of alteration at high temperature and pH: rates measurements and comparison with initial rates. *Procedia Mater. Sci.* **7**, 202–208 (2014).
36. Xiang, Y., Du, J., Smedskjaer, M. M. & Mauro, J. C. Structure and properties of sodium aluminosilicate glasses from molecular dynamics simulations. *J. Chem. Phys.* **139**, 044507 (2013).
37. Lu, X. et al. Effects of boron oxide substitution on the structure and bioactivity of SrO-containing bioactive glasses. *J. Mater. Sci.* **52**, 8793–8811 (2017).
38. Graves, G. N., Fontaine, A., Lagarde, P., Raoux, D. & Gurman, S. J. Local structure of silicate glasses. *Nature* **293**, 611–616 (1981).
39. McKeown, D. A., Waychunas, G. A. & Brown, G. E. Jr EXAFS and XANES study of the local coordination environment of sodium in a series of silica-rich glasses and selected minerals within the  $\text{Na}_2\text{O}-\text{Al}_2\text{O}_3-\text{SiO}_2$  system. *J. Non Cryst. Solids* **74**, 325–348 (1984).
40. Jollivet, P. et al. An enhanced resolution of the structural environment of zirconium in borosilicate glasses. *J. Non Cryst. Solids* **381**, 40–47 (2013).
41. Gambuzzi, E. et al. Probing silicon and aluminium chemical environments in silicate and aluminosilicate glasses by solid state NMR spectroscopy and accurate first-principles calculations. *Geochim. Cosmochim. Acta* **125**, 170–185 (2014).
42. Zapol, P., He, H., Kwon, K. D. & Criscenti, L. J. First-principles study of hydrolysis reaction barriers in a sodium borosilicate glass. *Int. J. Appl. Glass Sci.* **4**, 395–407 (2013).
43. Quintas, A. et al. NMR study of a rare-earth aluminoborosilicate glass with varying CaO-to-Na<sub>2</sub>O ratio. *Appl. Magn. Reson.* **32**, 613–634 (2007).
44. Chave, T., Frugier, P., Gin, S. & Ayrat, A. Glass-water interphase reactivity with calcium rich solutions. *Geochim. Cosmochim. Acta* **75**, 4125–4139 (2011).
45. Rimstidt, J. D. *Geochemical Rate Models: An Introduction to Geochemical Kinetics*. (Cambridge University Press, Cambridge, UK, 2014).
46. Chave, T., Frugier, P., Ayrat, A. & Gin, S. Solid state diffusion during nuclear glass residual alteration in solution. *J. Nucl. Mater.* **362**, 466–473 (2007).
47. Hench, L. L. *Sol-Gel Silica: Properties, Processing, and Technology Transfer* (Noyes Publications, Westwood, NJ, USA, 1998).
48. Ernsberger, F. M. Molecular water in glass. *J. Am. Ceram. Soc.* **60**, 91–92 (1977).
49. Wu, C.-K. Nature of incorporated water in hydrated silicate glasses. *J. Am. Ceram. Soc.* **63**, 453–457 (1980).
50. Newman, S., Stolper, E. & Epstein, S. Measurement of water in rhyolitic glasses: Calibration of an infrared spectroscopic technique. *Am. Mineral.* **71**, 1527–1541 (1986).
51. Sowerby, J. & Keppler, H. Water speciation in rhyolitic melt determined by in-situ infrared spectroscopy. *Am. Mineral.* **84**, 1843–1849 (1999).
52. Schmidt, B. C., Behrens, H., Riemer, T., Kappes, R. & Dupree, R. Quantitative determination of water speciation in aluminosilicate glasses: a comparative NMR and IR spectroscopic study. *Chem. Geol.* **174**, 195–208 (2001).
53. Yokoyama, T., Okumura, S. & Nakashima, S. Hydration of rhyolitic glass during weathering as characterized by IR microspectroscopy. *Geochim. Cosmochim. Acta* **72**, 117–125 (2008).
54. Brunet, F., Charpentier, T., Le Caer, S. & Renault, J. P. Solid-state NMR characterization of a controlled-pore glass and of the effects of electron irradiation. *Solid State Nucl. Magn. Reson.* **33**, 1–11 (2008).
55. Le Losq, C., Cody, G. D. & Mysen, B. O. Alkali influence on the water speciation and the environment of protons in silicate glasses revealed by  $^1\text{H}$  MAS NMR spectroscopy. *Am. Mineral.* **100**, 466–473 (2015).
56. Xue, X. & Kanzaki, M. Structure of hydrous aluminosilicate glasses along the diopside–anorthite join: a comprehensive one- and two-dimensional  $^1\text{H}$  and  $^{27}\text{Al}$  NMR study. *Geochim. Cosmochim. Acta* **72**, 2331–2348 (2008).
57. Smith, W. & Forester, T. DL-POLY\_2.0: A general-purpose parallel molecular dynamics simulation package. *J. Mol. Graph.* **14**, 136–141 (1996).
58. Fournier, M. et al. Glass dissolution rate measurement and calculation revisited. *J. Nucl. Mater.* **476**, 140–154 (2016).
59. Cailloteau, C. et al. Insight into silicate-glass corrosion mechanisms. *Nat. Mater.* **7**, 978–983 (2008).
60. Wild, B. et al. pH-dependent control of feldspar dissolution rate by altered surface layers. *Chem. Geol.* **442**, 148–159 (2016).
61. Aguiar, H., Serra, J., González, P. & León, B. Structural study of sol–gel silicate glasses by IR and Raman spectroscopies. *J. Non Cryst. Solids* **355**, 475–480 (2009).
62. Davis, K. M. & Tomozawa, M. An infrared spectroscopic study of water-related species in silica glasses. *J. Non Cryst. Solids* **201**, 177–198 (1996).
63. Larsen, F. H. & Farnan, I.  $^{29}\text{Si}$  and  $^{17}\text{O}$  (Q)CPMG-MAS solid-state NMR experiments as an optimum approach for half-integer nuclei having long T<sub>1</sub> relaxation times. *Chem. Phys. Lett.* **357**, 403–408 (2002).
64. Massiot, D. et al. Modelling one- and two-dimensional solid-state NMR spectra. *Magn. Reson. Chem.* **40**, 70–76 (2002).



**Open Access** This article is licensed under a Creative Commons Attribution 4.0 International License, which permits use, sharing, adaptation, distribution and reproduction in any medium or format, as long as you give appropriate credit to the original author(s) and the source, provide a link to the Creative Commons license, and indicate if changes were made. The images or other third party material in this article are included in the article's Creative Commons license, unless indicated otherwise in a credit line to the material. If material is not included in the article's Creative Commons license and your intended use is not permitted by statutory regulation or exceeds the permitted use, you will need to obtain permission directly from the copyright holder. To view a copy of this license, visit <http://creativecommons.org/licenses/by/4.0/>.

© The Author(s) 2018